Article

Not peer-reviewed version

Construction of TiO_2/LDHs Heterostructures with Interface Band Modulation and High-Efficiency Photodegradation of Methylene Blue

Jing Wei and Liying Ren *

Posted Date: 5 August 2025

doi: 10.20944/preprints202508.0262.v1

Keywords: photocatalysis; TiO2/LDHs; methylene blue; simulated solar irradiation

 doi:10.20944/preprints202508.0262.v1

Article

Construction of TiO_2/LDHs Heterostructures with Interface Band Modulation and High-Efficiency Photodegradation of Methylene Blue

Jing Wei and Liying Ren *

Shandong Provincial Key Laboratory of Soil Conservation and Environmental Protection, College of Resources and Environment, Linyi University, Linyi, 276000, China

* Correspondence: liyingren25@163.com

Abstract

TiO_2/LDHs composites were synthesized in different proportions using the co-precipitation method. Their structural characteristics, morphological characteristics and spectral responses were characterized by means of X-ray diffraction (XRD), raman spectra, scanning electron microscopy (SEM), transmission electron microscopy (TEM), and UV-vis diffuse reflectance spectroscopy. The photocatalytic performance of TiO_2/LDHs were tested with the degradation of methylene blue. The photocatalytic light source selected is simulated sunlight (300-watt xenon lamp). Experimental results demonstrate that constructing a robust heterojunction through precise interface band alignment significantly suppresses photogenerated electron-hole recombination. Controlled charge transfer pathways at the interface further enhance photocatalytic degradation efficiency. Among the tested catalysts, AT11 (Al:Ti=1:1, molar ratio) exhibits the highest photocatalytic activity, degrading 98.2% of methylene blue within 70 minutes under simulated solar irradiation. The degradation process follows first-order kinetics and maintains stable performance over four reuse cycles. Radical trapping experiments identify h^+ and ·OH as the dominant active species responsible for dye degradation. This TiO_2/LDHs heterostructure significantly enhances the photocatalytic efficiency of TiO_2, enabling efficient solar energy utilization.

Keywords: photocatalysis; TiO_2/LDHs; methylene blue; simulated solar irradiation

1. Introduction

Industrial advancement drives widespread use of synthetic dyes in textiles, food processing, paper manufacturing, and pharmaceuticals. These compounds persist as major wastewater pollutants due to molecular stability that resists standard treatments. Their polar groups enable water solubility while chromophores impart color, collectively posing severe ecological threats to aquatic systems through persistent contamination [1–4]. These dye-derived organic pollutants exhibit carcinogenic, mutagenic, and toxic properties. Untreated, they jeopardize human health and ecological integrity. Effective elimination of such compounds from wastewater is thus critical for pollution control. Recent decades have seen advanced treatment technologies emerge, including adsorption [5,6], biological degradation [7,8], electrocatalysis [9], and photocatalysis [10,11]. Heterogeneous photocatalysis has emerged as a leading strategy for wastewater remediation, leveraging potent oxidation power to mineralize diverse contaminants without secondary pollution. Its broad-spectrum efficacy against recalcitrant pollutants drives sustained research interest.

Conventional photocatalysts like TiO_2 demonstrate robust photocatalytic activity. Under light excitation, they generate electron-hole pairs whose oxidation potential drives dye degradation, specifically oxidizing adsorbed molecules on the catalyst surface [12–14]. However, TiO_2's practical utility is constrained by inherent limitations. Its wide bandgap (e.g., 3.2 eV in anatase phase) confines excitation to UV wavelengths, yielding negligible visible-light response and inefficient solar energy

 doi:10.20944/preprints202508.0262.v1

harvesting. Further, TiO_2 exhibits compromised photocatalytic efficiency due to synergistic limitations: weak surface adsorption capacity and rapid recombination of photogenerated charge carriers. These factors destabilize performance under operational conditions [15–18]. To enhance the photocatalytic performance of TiO_2, researchers employ three primary modification strategies: elemental doping [19–21], co-catalyst loading [22,23], and heterojunction engineering [24]. Among these approaches, constructing heterojunctions with semiconductors, particularly 2D layered materials possessing tailored band alignments, which proves highly effective for enhancing TiO_2 photocatalysis. This strategy promotes charge separation while suppressing carrier recombination [25–27]. Layered double hydroxides (LDHs) are a class of two-dimensional lamellar crystalline compounds classified as anionic clays. Their structure features hexagonal or octahedral crystalline frameworks defining characteristic interlayer galleries [28]. The general chemical formula of layered double hydroxides (LDHs) is given by $[M_{(1-x)}^{2+}M_x^{3+}(OH)_2]^{x+}(A^{n-})_{x/n}\cdot mH_2O$, where M^{2+} represents divalent cations (e.g., Ca^{2+}, Mg^{2+}, Fe^{2+}, Co^{2+}, Mn^{2+}, Cu^{2+}, Zn^{2+}, Ni^{2+}, etc.), M^{3+} denotes trivalent cations (e.g., Al^{3+}, Cr^{3+}, Fe^{3+}, Mn^{3+}, Co^{3+}, etc.), A^{n-} signifies interlayer anions (e.g., CO_3^{2-}, NO_3^-, SO_4^{2-}, Cl^-, etc.), and x represents the molar ratio of M^{2+} to M^{3+} [29,30]. LDHs feature expansive layered frameworks where bandgap engineering (2.0-3.4 eV) is achievable by varying M^{2+}/M^{3+} cations. This tunability enables effective construction of TiO_2 based photocatalytic heterojunctions, enhancing visible-light absorption while offering abundant surface active sites. LDHs shorten migration pathways for photogenerated carriers, suppressing charge recombination. This collective effect markedly enhances overall photocatalytic efficiency [31–34].

We synthesized TiO_2/LDHs composites with varied TiO_2 loading via MgAl-LDHs layer reconstruction. The materials' structure and morphology were characterized, while photocatalytic activity was assessed through methylene blue degradation under simulated sunlight. Reaction mechanisms were analyzed based on photocatalytic performance and radical trapping experiments.

2. Experimental

2.1. Synthesis of TiO_2/LDHs

2.1.1. Preparation of TiO_2 Sol

At room temperature, dissolve 4.4 mL butyl titanate in 26.4 mL anhydrous ethanol (Beaker A) with stirring. Separately, prepare Beaker B containing 1.32 mL triple-distilled water, 17.6 mL anhydrous ethanol, and 0.62 mL nitric acid. Using a peristaltic pump, add Solution B to Beaker A at 30 drops/min while vigorously stirring. After complete addition, continue stirring for 30 min to yield a milky TiO_2 sol.

2.1.2. Synthesis of LDHs Precursors

Under ambient temperature conditions, 12.80 g of magnesium nitrate hexahydrate ($Mg(NO_3)_2\bullet 6H_2O$) and 9.38 g of aluminum nitrate nonahydrate ($Al(NO_3)_3\cdot 9H_2O$) were weighed and dissolved in an appropriate amount of triple-distilled water in a beaker. According to the molar ratios of $n(OH^-)/ [n(Mg^{2+})+n(Al^{3+})]=2.2$ and $n(CO_3^{2-})/ [n(Mg^{2+})+n(Al^{3+})]=0.667$, 6.75 g of sodium hydroxide (NaOH) and 5.29 g of sodium carbonate (Na_2CO_3) were weighed and dissolved in another beaker. Both solutions were simultaneously added dropwise at a flow rate of 30 drops per minute into a beaker containing triple-distilled water, maintaining the system pH between 8 and 9. Using a low-temperature saturated co-precipitation method in a 60°C water bath, a hydrotalcite with a Mg:Al molar ratio of 2:1 was synthesized. The reaction mixture was continuously stirred during the process to obtain the desired LDHs precursor solution.

2.1.3. Synthesis of TiO_2/LDHs Nanocomposites

The LDHs precursor dispersion was stirred for 20 min before dropwise infusion of the TiO_2 sol. Continuous stirring (12 h) initiated crystallization, followed by a 6 h static aging stage. After

 doi:10.20944/preprints202508.0262.v1

centrifugation and washing to neutral pH, the precipitate was oven-dried at 80 °C. Subsequent grinding and calcination (500 °C, 2 h, air) yielded TiO_2/LDHs nanomaterial with Al:Ti = 1:1, labeled AT11. Identical procedures produced Al:Ti variants: 1:2 (AT12), 1:3 (AT13), 2:1 (AT21), and 3:1 (AT31).

2.2. Characterization

The phase and structural composition of the materials were analyzed through X-ray diffraction (XRD, D/MAX2500) and Raman spectroscopy (Horiba LabRAM HR Evolution). The microstructural morphology of the samples was characterized using scanning electron microscopy (SEM, ZEISS Sigma 360) and transmission electron microscopy (TEM, JEOL JEM-F200). The optical absorption properties and bandgap structure of the materials were evaluated via ultraviolet-visible diffuse reflectance spectroscopy (Shimadzu UV-3600i Plus).

2.3. Photocatalytic Experiments

The photocatalytic degradation of the target pollutant was conducted using a 15 mg/L methylene blue solution (150 mL) with a 300W xenon lamp as the light source and a catalyst concentration of 1 g/L. Prior to initiating the reaction, the mixture was stirred in the dark for 20 minutes to achieve adsorption equilibrium between the catalyst and the methylene blue solution. Throughout the photocatalytic experiment, magnetic stirring was maintained, and samples were collected every 10 minutes. After centrifugation, the supernatant was analyzed for absorbance. A spectrophotometer was employed to measure the absorbance of methylene blue solutions at various concentrations at 665 nm, the maximum absorption wavelength of methylene blue. The absorbance-concentration standard curve was plotted, and through linear fitting, the standard curve equation was obtained as follows:

$$y = 0.0716x + 0.0542, R^2 = 0.9992 \quad (1)$$

3. Results and Discussion

3.1. Material Characterization and Analysis

3.1.1. X-Ray Powder Diffraction

To determine the crystal structure and characteristics of the composite materials, XRD analysis was conducted on TiO_2, LDHs, and AT11, with the results presented in Figure 1. The pure TiO_2 material exhibited diffraction peaks at 2θ values of 25.30°, 37.79°, 48.04°, 53.88°, 55.07°, and 62.69°, corresponding to the (101), (004), (200), (105), (211), and (204) crystal planes of anatase TiO_2 (JCPDS: 71-1166), respectively [35]. LDHs showed prominent diffraction peaks at 2θ values of 46.99° and 62.13°, which align with the characteristic peaks of the standard card $Mg_{0.67}Al_{0.33}(OH)_2(CO_3)_{0.165}(H_2O)_{0.48}$ (JCPDS: 89-5434), corresponding to the (018) and (113) crystal planes of LDHs [35]. In the XRD pattern of the AT11 composite, the primary diffraction peaks observed for TiO_2 were associated with the (101) plane, while those for LDHs were linked to the (018) and (113) planes. Additionally, two new diffraction peaks appeared in the AT11 composite at 2θ values of 18.18° and 32.55°, consistent with the characteristic peaks of $(MgTi)_2O_5$ (JCPDS: 82-1125), corresponding to its (200) and (203) crystal planes. This indicates that the AT11 composite not only contains the TiO_2 and LDHs phases but also forms a new crystalline phase structure.

 doi:10.20944/preprints202508.0262.v1

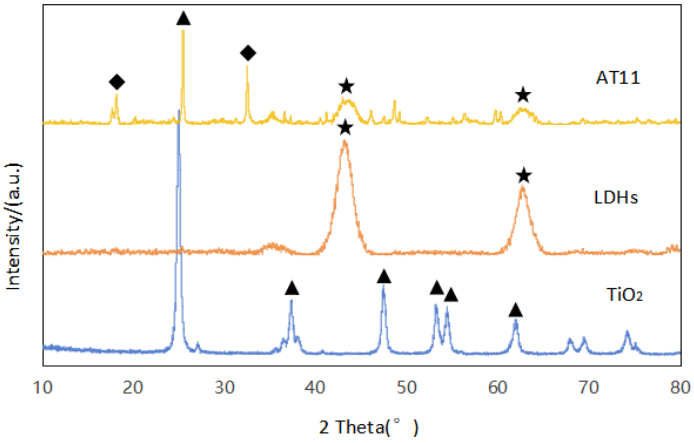

Figure 1. XRD patterns of TiO_2, LDHs and AT11.

3.1.2. Morphological Analysis of TiO_2/LDHs

The microstructure and morphology of the TiO_2/LDHs composite were investigated using SEM and TEM, as illustrated in Figure 2. Figures 2a and 2b reveal the layered structure of LDHs and the lattice fringes of TiO_2, with the average particle size of AT11 ranging between 20 and 30 nm. The particle distribution is relatively uniform, although significant agglomeration is observed. Figure 2c demonstrates that the composite exhibits an irregular polygonal structure, with TiO_2 nanoparticles dispersed within the LDHs lamellar structure [35]. This indicates that the layered architecture provides abundant loading sites for TiO_2 particles [36]. Such structural modifications are hypothesized to enhance the photocatalytic activity of the composite, a supposition subsequently validated by the results of photocatalytic experiments.

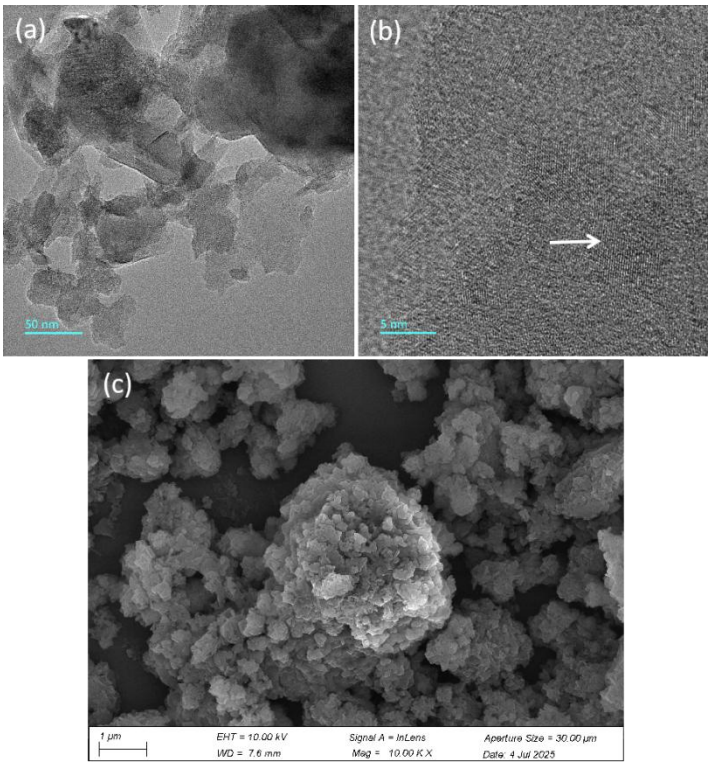

Figure 2. The microscopic morphology of the materials: (a) and (b) AT11(TEM); (c) AT11(SEM).

3.1.3. Raman Spectroscopy

 doi:10.20944/preprints202508.0262.v1

The Raman spectrum of the AT11 composite material is illustrated in Figure 3. As depicted, the absorption peak at 1065 cm^{-1} is attributed to the characteristic stretching vibration of CO_3^{2-} within the interlayer of LDHs [19]. The absorption peak at 846 cm^{-1} corresponds to NO_3^-, which is a residue from the decomposition of the precursor. The peak at 777 cm^{-1} is assigned to the Ti-O-Ti vibration, indicating the successful loading of TiO_2 on the surface of LDHs [37]. The peak at 655 cm^{-1} reflects the interfacial coupling vibration of Ti-O-M (M=Mg/Al), demonstrating the bonding interaction within the heterostructure. In conjunction with the characteristic peaks at 18.18° and 32.55° observed in the XRD characterization of AT11, this peak is identified as the interfacial bonding vibration of Ti-O-Mg [38]. The peaks at 487cm^{-1}, 428cm^{-1}, and 385 cm^{-1} represent the υ_3/υ_4 vibrational characteristics of the tetrahedral [MO_4] groups, indicating the presence of a defect structure with coexisting tetrahedral and octahedral configurations in the composite material. This structure, induced by anion intercalation or synthesis conditions, can optimize the material's photocatalytic, adsorption, and ion exchange properties [25,39]. The peak at 256 cm^{-1} is attributed to the vibration of Ti-O-Al or Ti-O-Mg. The peak at 161 cm^{-1} is identified as the B_{1g} vibrational mode of anatase TiO_2, reflecting the symmetric stretching vibration of the Ti-O bond in the TiO_2 crystal. Although the typical B_{1g} peak of anatase TiO_2 is located near 144 cm^{-1}, the shift to 161 cm^{-1} may be due to specific microstructural features of the sample, such as tensile stress introduced by heterointerfaces or surface defects. In summary, these findings demonstrate that TiO_2 has been successfully loaded onto the surface of LDHs, forming a heterostructure that enhances the material's photocatalytic, adsorption, and ion exchange properties.

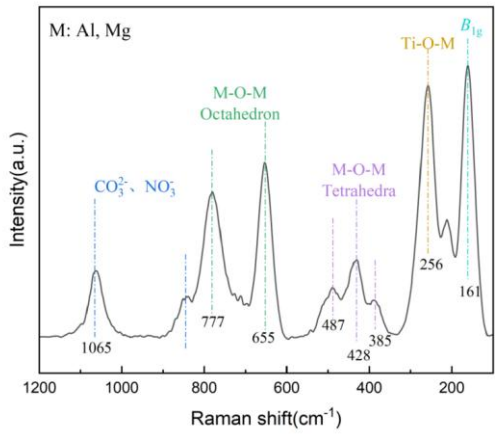

Figure 3. The Raman spectroscopy spectrum of AT11.

3.1.4. UV-Vis Diffuse Reflectance Spectroscopy

To investigate the optical properties of composite materials, ultraviolet-visible diffuse reflectance spectroscopy was performed on TiO_2 and AT11, with the results presented in Figure 4. The data reveals that TiO_2 exhibits a UV response exclusively, with an absorption edge at 400 nm. In contrast, AT11 demonstrates an extended absorption edge reaching 500 nm. This indicates that the composite formation between TiO_2 and LDHs establishes an efficient heterojunction structure through interfacial band alignment. The LDHs layer consists of tunable metal elements, typically possessing a conduction band position higher than that of TiO_2 and a valence band position significantly lower than TiO_2. This band arrangement forms a Type-II heterojunction at the interface, facilitating the migration of photogenerated electrons from the LDHs conduction band to the TiO_2 conduction band, while simultaneously transferring holes from the TiO_2 valence band to the LDHs valence band. This process not only effectively suppresses carrier recombination but also extends the photoresponse range of the composite material into the visible light region through the narrow bandgap characteristics of LDHs [40].

 doi:10.20944/preprints202508.0262.v1

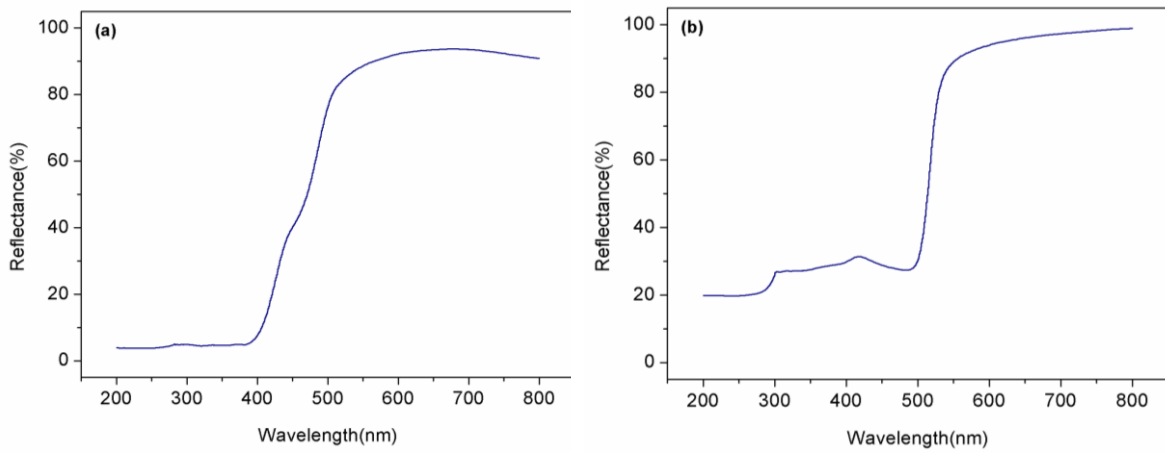

Figure 4. The UV-Vis Spectra of the materials: (a) TiO_2; (b) AT11.

3.2. Photocatalytic Performance of Photocatalysts

3.2.1. Impact of Diverse Composite Materials on Photocatalytic Performance

This study investigated the photocatalytic degradation efficiency of TiO_2/LDHs composite materials (AT11, AT12, AT13, AT21, AT31) with varying content ratios under simulated sunlight, using methylene blue as the target pollutant, as illustrated in Figure 5. The experimental procedure involved a 20-minute dark reaction to achieve adsorption-desorption equilibrium of the catalyst prior to photocatalytic testing. The results demonstrate that pure TiO_2 photocatalyst exhibits minimal adsorption capacity for methylene blue, while the composite photocatalysts show progressively enhanced adsorption with increasing LDHs content. However, the adsorption rate significantly decelerates when the Al:Ti molar ratio exceeds 1:1. Photocatalytic reaction analysis reveals that all TiO_2/LDHs composites exhibit substantially higher photocatalytic activity compared to pure TiO_2. The photocatalytic degradation efficiency initially increases and subsequently decreases with rising LDHs content, reaching optimal performance at an Al:Ti molar ratio of 1:1 (AT11), achieving a remarkable 98.20% degradation rate of methylene blue within 70 minutes of reaction.

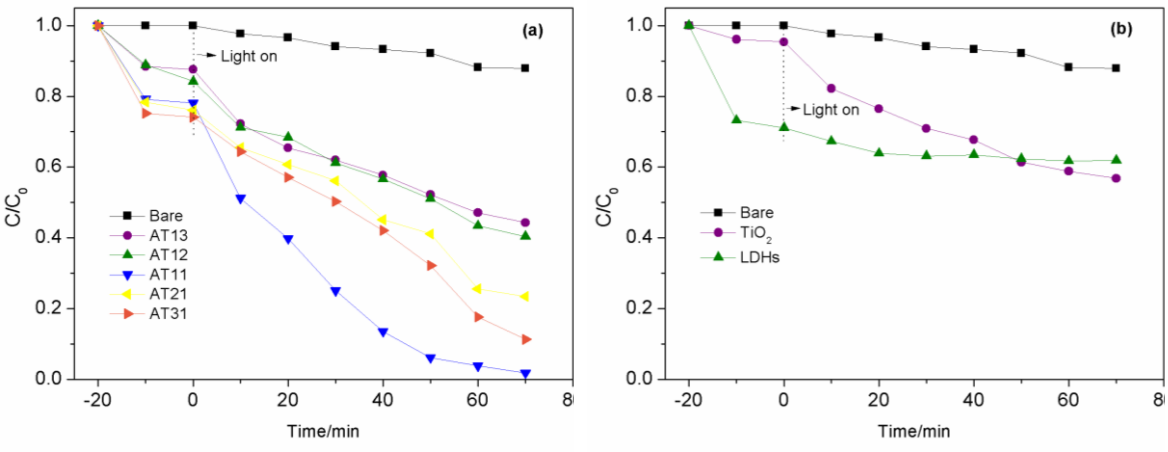

Figure 5. Degradation effect of different photocatalytic materials on methylene blue.

Based on the aforementioned results, the TiO_2/LDHs composite material exhibits superior adsorption capabilities, which enhance the direct contact efficiency between the target degradation molecules, their photocatalytic oxidation intermediates, and the photogenerated holes on the composite surface. This synergistic effect of adsorption and photocatalysis significantly improves the overall photocatalytic efficiency. Furthermore, during the material compounding process, TiO_2 is embedded into the LDHs layers and pores, ensuring its uniform dispersion on the LDHs carrier. This

 doi:10.20944/preprints202508.0262.v1

provides more active sites for photocatalytic reactions, reduces the agglomeration and shielding of photocatalytic active particles, and enhances the overall photocatalytic reaction efficiency. When the proportion of LDHs in the composite material is relatively low, TiO_2 can be uniformly distributed on the surface and interlayer of LDHs. However, with the continuous increase in LDHs content, the excessive LDHs lead to a relative reduction in active sites on the surface of the composite material, resulting in a decrease in its photocatalytic efficiency.

3.2.2. Kinetic Analysis of Photocatalytic Reactions

The photocatalytic degradation data were fitted using a pseudo-first-order kinetic model, with the results presented in Table 1 and Figure 6. The fitting results indicate that the linear correlation coefficients for all catalysts exceed 0.95, demonstrating that their photocatalytic degradation processes conform to the pseudo-first-order reaction kinetic model. Among them, AT11 exhibits the highest photocatalytic reaction rate constant of 0.0543 min^{-1}, which is 7.5 times that of pure TiO_2, thereby substantiating a significant enhancement in photocatalytic activity upon the combination of TiO_2 with LDHs.

Table 1. Kinetic Parameters of Photocatalytic Degradation of Methylene Blue.

Sample	K/min^{-1}	R^2
TiO_2	0.007 2	0.968 7
AT13	0.009 1	0.976 6
AT12	0.010 2	0.987 5
AT11	0.054 3	0.980 5
AT21	0.016 8	0.965 4
AT31	0.027 0	0.969 6

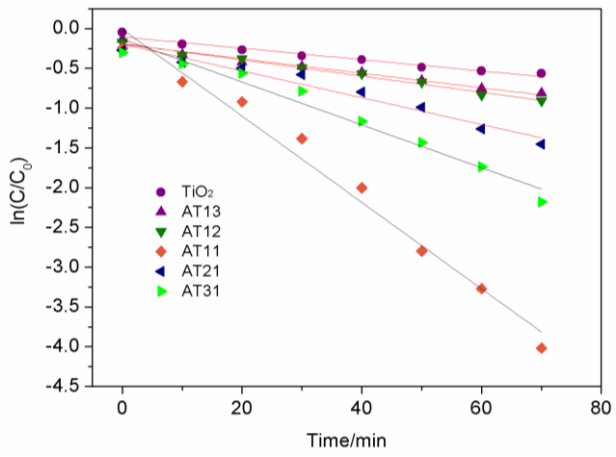

Figure 6. Pseudo-first-order kinetic fitting curve for photocatalytic degradation of methylene blue.

3.2.3. The Impact of Catalyst Concentration on Photocatalytic Performance

The experiment employed AT11 composite material as the catalyst, maintaining identical reaction conditions and procedures as the aforementioned photocatalytic process. The photocatalytic reaction was conducted for 70 minutes to investigate the impact of varying catalyst concentrations on the degradation of methylene blue. The results are illustrated in Figure 7.

 doi:10.20944/preprints202508.0262.v1

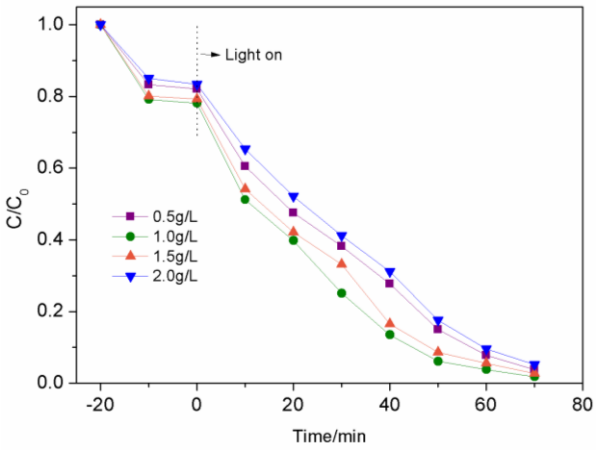

Figure 7. The Impact of Catalyst Concentration on Methylene Blue Degradation.

As clearly illustrated in the figure, when the catalyst concentration is below 1 g/L, the degradation rate of methylene blue exhibits an increasing trend with the elevation of catalyst concentration. The augmentation of catalyst concentration facilitates the adsorption of more reactants on the catalyst surface, thereby enhancing light absorption and improving the generation rate of photogenerated holes, which consequently promotes the photocatalytic reaction. The maximum degradation rate of methylene blue is achieved at a catalyst concentration of 1 g/L. However, when the catalyst concentration exceeds 1 g/L, the degradation rate of methylene blue gradually decreases with the increase of catalyst dosage. This phenomenon can be attributed to the shielding effect of excessive catalyst on incident light, which adversely affects the transmittance of the reaction solution and consequently reduces the generation rate of photogenerated holes. Therefore, under the experimental conditions of this study, the optimal catalyst concentration is determined to be 1 g/L.

3.2.4. The Impact of Inorganic Anions on Photocatalytic Reactions

This study selected Cl^-, NO_3^-, SO_4^{2-}, and CO_3^{2-} as representative inorganic anions to investigate their impact on the photocatalytic degradation of methylene blue. Using AT11 as the catalyst at a concentration of 1g/L, the experiments were conducted with the addition of 5mmol/L NaCl, $NaNO_3$, Na_2SO_4, and $NaCO_3$ respectively. The photocatalytic reactions were carried out for 70 minutes, and the results are presented in Figure 8. As illustrated in Figure 8, Cl^-, NO_3^-, and SO_4^{2-} exhibit minimal impact on the degradation of methylene blue within the system, whereas CO_3^{2-} demonstrates a significant inhibitory effect on the photodegradation of methylene blue. This phenomenon can be attributed to the weak acidity of CO_3^{2-}, which, upon hydrolysis in aqueous solution, readily combines with hydrogen ions to form HCO_3^- and OH^-. Subsequently, HCO_3^- reacts with active species such as ·OH generated during the photocatalytic process, resulting in the formation of carbonate compounds. These compounds further cover the active sites, thereby reducing the catalytic activity.

 doi:10.20944/preprints202508.0262.v1

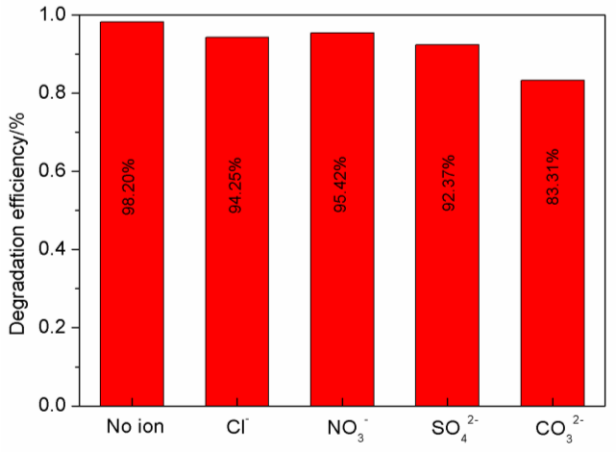

Figure 8. Effect of Coexisting Anions on the Degradation of Methylene Blue by AT11.

3.2.5. Free Radical Trapping Experiment

The primary active species in photocatalytic oxidation reactions include photogenerated holes (h^+), hydroxyl radicals (·OH), and superoxide radicals (·O^{2-}). To investigate the photocatalytic oxidation mechanism of methylene blue by TiO_2/LDHs composite materials, sodium bicarbonate [41] ($NaHCO_3$, h^+ scavenger), isopropanol [42] (IPA, ·OH scavenger), and p-benzoquinone [43] (BQ, ·O^{2-} scavenger) were introduced into the reaction system, respectively. Photocatalytic experiments were conducted under identical reaction conditions using AT11 as the catalyst, and the results are presented in Figure 9. As illustrated in Figure 9, the degradation efficiency of AT11 towards methylene blue decreased to 54.52%, 68.10%, and 87.63% upon the addition of $NaHCO_3$, IPA, and BQ, respectively. This indicates that all three reactive species play significant roles in the photocatalytic degradation of methylene blue. Specifically, h^+ and ·OH are identified as the primary reactive species responsible for the degradation, while ·O^{2-} exhibits a limited influence on the photocatalytic reaction process.

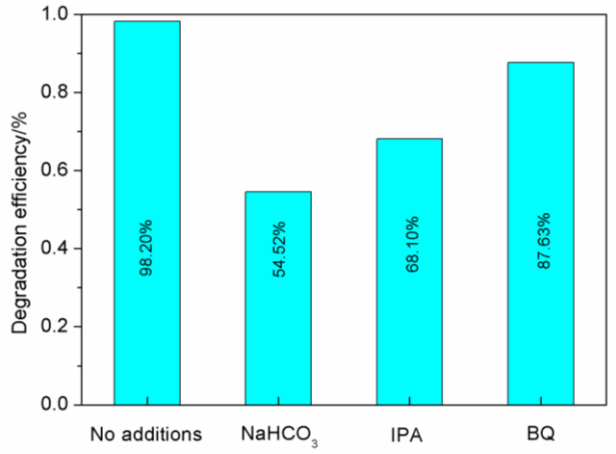

Figure 9. Free Radical Trapping Experiment.

3.2.6. Evaluation of Photocatalytic Stability in Composite Materials

The reusability of photocatalytic materials constitutes a critical factor in assessing the stability of catalyst performance. This study conducted four consecutive cycling experiments on AT11 to evaluate its photocatalytic degradation efficiency of methylene blue, with the results illustrated in Figure 10. The data demonstrate that after four cycles of reuse, the degradation efficiency of AT11 for methylene blue decreased from 98.20% to 78.93%, indicating relatively favorable stability of the

 doi:10.20944/preprints202508.0262.v1

catalyst. The observed decline in activity may be attributed to two primary factors: minor sample loss during the recovery and washing processes, and the partial coverage of catalyst surface pores by reactants and products during the reaction, leading to the deactivation of active sites and subsequent reduction in degradation efficiency.

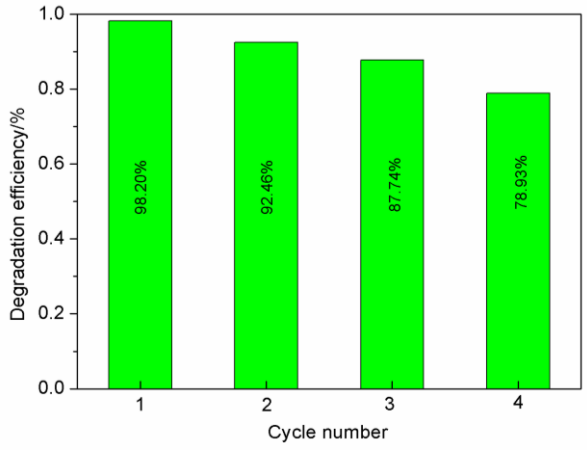

Figure 10. Recycling of AT11 composites.

4. Conclusions

TiO_2/LDHs composite materials with varying Al/Ti molar ratios were synthesized via the co-precipitation method. The formation of an efficient heterojunction structure through interfacial band alignment effectively suppressed carrier recombination and extended the photoresponse range of the composite materials into the visible light spectrum. The AT11 composite demonstrated optimal performance, achieving a 98.20% degradation rate of methylene blue (15 mg/L) under simulated sunlight irradiation for 70 minutes. The photocatalytic reaction followed first-order kinetics with a rate constant of 0.0543 min^{-1}. After four consecutive cycles, the AT11 composite maintained a methylene blue degradation efficiency of 78.93%, exhibiting excellent stability.

The composite of TiO_2 with LDHs demonstrates superior photocatalytic performance due to the synergistic effects of different catalyst components and modifications in the band structure. LDHs significantly enhance the adsorption capacity of the composite while mitigating the agglomeration of TiO_2, thereby providing more effective active sites for the reaction and substantially improving the efficiency of photocatalytic degradation. Radical trapping experiments reveal that the primary active species responsible for the photocatalytic degradation of methylene blue by TiO_2/LDHs are h^+ and ·OH.

Author Contributions: Conceptualization, J.W. and L.R.; methodology, J.W. and L.R.; formal analysis, J.W.; data curation, J.W. and L.R.; writing—original draft preparation, J.W.; writing—review and editing, L.R. All authors have read and agreed to the published version of the manuscript.

Funding: This research was funded by "Key Research and Development Program Project of Shandong Province", grant number 2024TSGC0884 .

Data Availability Statement: Data are available from the corresponding author upon reasonable request.

Acknowledgments: The authors acknowledge the financial support through Key Research and Development Program Project of Shandong Province, number (2024TSGC0884), Shandong, China.

Conflicts of Interest: The authors declare no conflicts of interest.

References

 doi:10.20944/preprints202508.0262.v1

1. Guo, J.; Zhou, T. T.; Guo, H.; Ge, C.; Lu, J. J. Application of nano-TiO_2@adsorbent composites in the treatment of dye wastewater: A review. *Journal Of Engineered Fibers And Fabrics* **2025**, 20, 15589250251329450. DOI: 10.1177/15589250251329450
2. Chang, Q.; Jiang, G.D.; Hu, M.X.; Huang, J.; Tang, H.Q. Adsorption of Methylene Blue from Aqueous Solution onto Magnetic Fe_3O_4 / Graphene Oxide Nanoparticles. *Environmental Science* **2014**, 35(5), 1804–1809 (in Chinese). DOI: 10.13227/j.hjkx.2014.05.024
3. Willison, E.O.C.; Lopes, A.S.C.; Monteiro, W.R.; Filho, G.N.R.; Nobre, F.X.; Luz, P.T.S.; Nascimento, L.A.S.; Costa, C.E.F.; Monteiro, W.F.; Vieira, M.O.; Zamian, J.R. Layered double hydroxides as heterostructure LDH@Bi_2WO_6 oriented toward visible-light-driven applications: synthesis, characterization, and its photocatalytic properties. *Reaction Kinetics, Mechanisms and Catalysis* **2020**, 131, 505–524. https://doi.org/10.1007/s11144-020-01830-8
4. Fadzli, J.; Hamid, K.H.K.; Him, N.R.N.; Puasa, S.W. A critical review on the treatment of reactive dye wastewater. *Desalination And Water Treatment* **2022**, 257, 185-203. DOI: 10.5004/dwt.2022.28028
5. Li, Z.J.; Sun, Y.K.; Xing, J.; Meng, A. Fast removal of Methylene Blue by Fe_3O_4 magnetic nanoparticles and their cycling property. *Journal Of Nanoscience And Nanotechnology* **2019**,19(4), 2116-2123. DOI: 10.1166/jnn.2019.15809
6. Kang, J.Y.; Deng, S.; Han, X.; Wu, S.X.; Bai, Y.Y.; Jiang, Y.H.; Yang, Y. Adsorption Properties and Mechanism of Ciprofloxacin Enhanced by Mn-Doped Biochar. *Research of Environmental Sciences* **2024**, 37(11), 2526-2536 (in Chinese). DOI: 10.13198/j.issn.1001-6929.2024.09.03
7. Kim, Y.K.; Yoo, K.; Kim, M.S.; Han, I.; Lee, M.; Kang, B.R.; Lee, T.K.; Park, J. The capacity of wastewater treatment plants drives bacterial community structure and its assembly. *Scientific Reports* **2019**, 9, 14809. DOI: 10.1038/s41598-019-50952-0
8. Assress, H.A.; Selvarajan, R.; Nyoni, H.; Ntushelo, K.; Mamba, B.B.; Msagati, T.A.M.Diversity, co-occurrence and implications of fungal communities in wastewater treatment plants. *Scientific Reports* **2019**, 9, 14056. DOI: 10.1038/s41598-019-50624-z
9. Das, S.; Ghangrekar, M.M. Tungsten oxide as electrocatalyst for improved power generation and wastewater treatment in microbial fuel cell. *Environmental Technology* **2020**, 41(19), 2546-2553. DOI: 10.1080/09593330.2019.1575477
10. Nobre, F.X.; Pessoa, W.A.; Ruiz, Y.L.; Bentes, V.L.I.; Silva-Moraes, M.O.; Silva, T.M.C.; Rocco, M.L.M.; Larrudé, D.R.G.; de Matos, J.M.E.; Couceiro, P.R.D. Facile synthesis of nTiO_2 phase mixture: characterization and catalytic performance. *Materials Research Bulletin* **2019**, 109, 60-71. DOI: 10.1016/j.materresbull.2018.09.019
11. Bodzek, M.; Konieczny, K.; Kwiecinska-Mydlak, A. Nano-photocatalysis in water and wastewater treatment. *Desalination And Water Treatment* **2021**, 243, 51-74. DOI: 10.5004/dwt.2021.27867
12. Kumar, S.; Chanana, A. TiO_2 based nanomaterial: Synthesis, structure, photocatalytic properties, and removal of dyes from wastewater. *Korean Journal Of Chemical Engineering* **2023**, 40(8), 1822-1838. DOI: 10.1007/s11814-023-1455-6
13. Liang, S.X.; Zhang, Y.H.; Sun, Z.C.; Chang, Y.K. Laboratory study on the evolution of waves parameters due to wave breaking in deep water. *Wave Motion* **2017**, 68, 31-42. DOI: 10.1016/j.wavemoti.2016.08.010
14. Njema, G.G.; Kibet, J.K. A review of novel materials for nano-photocatalytic and optoelectronic applications: Recent perspectives, water splitting and environmental remediation. *Progress in Engineering Science* **2024**, 1(4), 100018. https://doi.org/10.1016/j.pes.2024.100018
15. Chen, J.R.; Qiu, F.X.; Xu, W.Z.; Cao, S.S.; Zhu, H.J. Recent progress in enhancing photocatalytic efficiency of TiO_2-based materials. *Applied Catalysis A-General* **2015**, 495, 131-140. DOI: 10.1016/j.apcata.2015.02.013
16. Chen, S.Q.; Hu, Y.H. Color TiO_2 Materials as Emerging Catalysts for Visible-NIR Light Photocatalysis, A Review. *Catalysis Reviews-Science And Engineering* **2023**, 66(5), 1951-1991. DOI: 10.1080/01614940.2023.2169451
17. Guo, Q.; Zhou, C.Y.; Ma, Z.B.; Yang, X.M. Fundamentals of TiO_2 Photocatalysis: Concepts, Mechanisms, and Challenges. *Advanced Materials* **2019**, 31(50), 1901997. DOI: 10.1002/adma.201901997

 doi:10.20944/preprints202508.0262.v1

18. Peiris, S.; de Silva, H.B.; Ranasinghe, K.N.; Bandara, S.V.; Perera, I.R. Recent development and future prospects of TiO_2 photocatalysis. *Journal Of The Chinese Chemical Society* **2021,** 68(5), 738-769. DOI: 10.1002/jccs.202000465
19. Fernandes, E.; Gomes, J.; Martins, R.C. Semiconductors Application Forms and Doping Benefits to Wastewater Treatment: A Comparison of TiO_2, WO_3, and g-C_3N_4. *Catalysts* **2022**, 12(10), 1218. DOI: 10.3390/catal12101218
20. Sari, Y.; Gareso, P.L.; Tahir, D. Review: influence of synthesis methods and performance of rare earth doped TiO_2 photocatalysts in degrading dye effluents. *International Journal Of Environmental Science And Technology* **2025**, 22(3), 1975-1994. DOI: 10.1007/s13762-024-05879-z
21. Chao, L.; Wang, Z.X.; He, J.R. Photocatalytic Oxidation of Printing and Dyeing Wastewater by Foam Ceramics Loaded with Cu and N-TiO_2. *Catalysis Letters* **2024**, 154(7), 3937-3946. DOI: 10.1007/s10562-024-04614-0
22. Indira, A.C.; Muthaian, J.R.; Pandi, M.; Mohammad, F.; Al-Lohedan, H.A.; Soleiman, A.A. Photocatalytic Efficacy and Degradation Kinetics of Chitosan-Loaded Ce-TiO_2 Nanocomposite towards for Rhodamine B Dye. *Catalysts* **2023**, 13(12), 1506. DOI: 10.3390/catal13121506
23. Tiwari, V.; Pal, B.; Kaur, S. Photocatalysis of Ag-loaded $MgTiO_3$ for degradation of fuchsin dye and dyes present in textile wastewater under sunlight. *Solar Energy* **2025**, 296, 113587. DOI: 10.1016/j.solener.2025.113587
24. Li, Y.; Zhang, M.Q.; Liu, Y.F.; Sun, Y.X.; Zhao, Q.H.; Chen, T.L.; Chen, Y.F.; Wang, S.F. In Situ Construction of Bronze/Anatase TiO_2 Homogeneous Heterojunctions and Their Photocatalytic Performances. *Nanomaterials* **2022**, 12(7), 1122. DOI: 10.3390/nano12071122
25. Xu, S. W.; Li, Z. W.; Wen, J. H.; Qiu, P.; Xie, A. J.; Peng, H. P. Review of TiO_2-Based Heterojunction Coatings in Photocathodic Protection. *Acs Applied Nano Materials* **2024**, 7(8), 8464-8488. DOI: 10.1021/acsanm.4c00541
26. Du, M.Q.; Cao, S.X.; Ye, X.Z.; Ye, J.F. Recent Advances in the Fabrication of All-Solid-State Nanostructured TiO_2-Based Z-Scheme Heterojunctions for Environmental Remediation. *Journal Of Nanoscience And Nanotechnology* **2020**, 20(9), 5861-5873. DOI: 10.1166/jnn.2020.18719
27. Wu, X.H.; Chen, G.Q.; Wang, J.; Li, J.M.; Wang, G.H. Review on S-Scheme Heterojunctions for Photocatalytic Hydrogen Evolution. *Acta Physico-Chimica Sinica* **2023**, 39(6), 2212016. DOI: 10.3866/PKU.WHXB202212016
28. Ye, D.; Sun, L.; Feng, J.Y.; Gao, S.J.; Zhu, K.; Wu, K.; Guo, R.T. Progress on photocatalytic elimination of CO_2 and gaseous pollutants over LDHs-based materials. *Journal Of Industrial And Engineering Chemistry* **2025**, 144, 175-191. DOI: 10.1016/j.jiec.2024.10.007
29. Wang, Y.Z.; Wang, S.; Li, X.L.; Bai, P.; Yan, W.F.; Yu, J.H. Layered Inorganic Cationic Frameworks beyond Layered Double Hydroxides (LDHs): Structures and Applications. *European Journal Of Inorganic Chemistry* **2020**, 43, 4055-4063. DOI: 10.1002/ejic.202000710
30. Chang, Q.F.; Zhang, X.L.; Wang, B.; Niu, J.T.; Yang, Z.X.; Wang, W.C. Fundamental understanding of electrocatalysis over layered double hydroxides from the aspects of crystal and electronic structures. *Nanoscale* **2022**, 14(4), 1107-1122. DOI: 10.1039/d1nr07355a
31. Hadnadjev-Kostic, M.; Vulic, T.; Lukic, N.; Jokic, A.; Karanovic, D. Photocatalytic Performance of TiO_2-ZnAl LDH Based Materials: Kinetics and Neural Networks Approach. *Polish Journal Of Environmental Studies* **2022**, 31(5), 4117-4125. DOI: 10.15244/pjoes/147023
32. Mohapatra, L.; Parida, K. A Review on Recent Progress, Challenges and Perspective of Layered Double Hydroxides as Promising Photocatalysts. *Journal Of Materials Chemistry A* **2016**, 4(28), 10744-10766. DOI: 10.1039/c6ta01668e
33. Wang, L.Y.; Gao, X.; Cheng, Y.Q.; Zhang, X.X.; Wang, G.Q.; Zhang, Q.Y.; Su, J.X. TiO_2@MgAl-layered double hydroxide with enhanced photocatalytic activity towards degradation of gaseous toluene. *Journal Of Photochemistry And Photobiology A-Chemistry* **2019**, 369, 44-53. DOI: 10.1016/j.jphotochem.2018.10.004
34. Suh, M.J.; Shen, Y.; Chan, C.K.; Kim, J.H. Titanium Dioxide-Layered Double Hydroxide Composite Material for Adsorption-Photocatalysis of Water Pollutants. *Langmuir* **2019**, 35(26), 8699-8708. DOI: 10.1021/acs.langmuir.9b00539

 doi:10.20944/preprints202508.0262.v1

35. Gao, X.; Zheng, K.; Zhang, Q.; Cao, X.; Wu, S.; Su, J. Self-assembly TiO_2-RGO/LDHs nanocomposite: Photocatalysis of VOCs degradation in simulation air. *Applied Surface Science* **2022**, 586, 152882. https://doi.org/10.1016/j.apsusc.2022.152882
36. Wang, Z.; Sun, Y.; Zhao, X.; Zhang, K.; Wang, X.; Liu, C.; Cui, J. Construction of two-dimensional nano-composite g-C_3N_4/LDHs and photocatalytic degradation of ciprofloxacin. *Applied Chemical Industry* **2025**, 54(4), 881-886, 894. DOI:10.16581/j.cnki.issn1671-3206.2025.04.001
37. Seftel, E.M.; Niarchos, M.; Mitropoulos, C.; Mertens, M.; Vansant, E.F.; Cool, P. Photocatalytic removal of phenol and methylene-blue in aqueous media using TiO_2@LDH clay nanocomposites. *Catalysis Today*, **2015**, 252, 120-127. https://doi.org/10.1016/j.cattod.2014.10.030
38. Singh R.; Biswas K. Synthesis optimization and investigation on electrical properties of Fe^{2+}-doped Mg_2TiO_4 ceramics for energy storage. *Journal of Materials Science: Materials in Electronics* **2020**, 31(15), 12434-12443. https://doi.org/10.1007/s10854-020-03790-0
39. Khan, M. A.; Fattah-alhosseini, A.; Kaseem, M. Recent advances in the design and surface modification of titanium-based LDH for photocatalytic applications. *Inorganic Chemistry Communications* **2023**, 153, 110739. DOI: 10.1016/j.inoche.2023.110739
40. Miljevic, B.; van der Bergh, J. M.; Vucetic, S.; Lazar, D.; Ranogajec, J. Molybdenum doped TiO_2 nanocomposite coatings Visible light driven photocatalytic self-cleaning of mineral substrates. *Ceramics International* **2017**, 43(11), 8214-8221. DOI: 10.1016/j.ceramint.2017.03.149
41. Hassani, A.; Eghbali, P.; Mahdipour, F.; Waclawek, S.; Lin, K. Y. A.; Ghanbari, F. Insights into the synergistic role of photocatalytic activation of peroxymonosulfate by UVA-LED irradiation over $CoFe_2O_4$-rGO nanocomposite towards effective Bisphenol A degradation: Performance, mineralization, and activation mechanism. *Chemical Engineering Journal* **2022**, 453, 139556. DOI: 10.1016/j.cej.2022.139556
42. Xie, W. J.; Zhang, Y.; Xu, L.; Xie, D.; Jiang, L.; Dong, Y. M.; Yuan, Y. Degradation of Organic Dyes by the UCNP/h-BN/TiO_2 Ternary Photocatalyst. *Acs Omega* **2023**, 8(51), 48662-48672. DOI: 10.1021/acsomega.3c01899
43. Rao, L. J.; Yang, Y. F.; Chen, L. K.; Liu, X. D.; Chen, H. X.; Yao, Y. Y.; Wang, W. T. Highly efficient removal of organic pollutants via a green catalytic oxidation system based on sodium metaborate and peroxymonosulfate. *Chemosphere* **2020**, 238, 124687. DOI: 10.1016/j.chemosphere.2019.124687